



# COMPACTION-INDUCED NON-MONOTONIC VARIATION OF LONGITUDINAL DISPERSION COEFFICIENT IN GRANULAR MEDIA

Yang Liu , Wenbo Gong, Han Xiao, Moran Wang 

*Department of Engineering Mechanics, Tsinghua University, Beijing, China*

**Correspondence to:**

Moran Wang at  
[mrwang@tsinghua.edu.cn](mailto:mrwang@tsinghua.edu.cn)

**How to Cite:**

Liu, Y., Gong, W., Xiao, H., & Wang, M. (2025).  
Compaction-Induced  
Non-Monotonic Variation  
of Longitudinal Dispersion  
Coefficient in Granular  
Media. *InterPore Journal*,  
2(4), IPJ011225-2.  
<https://doi.org/10.69631/an65j282>

RECEIVED: 26 Nov. 2024

ACCEPTED: 1 Oct. 2025

PUBLISHED: 1 Dec. 2025

**ABSTRACT**

This study numerically investigates the impact of compaction on the longitudinal dispersion coefficient of granular materials by integrating the discrete element method with the pore network model. The results reveal a non-monotonic relationship between the dispersion coefficient and compaction. Specifically, the dispersion coefficient can decrease by up to 20% or increase by nearly 50% in magnitude. Furthermore, we define the variation in the dispersion coefficient, denoted as  $\kappa$ , which exhibits three distinct regimes across different Péclet numbers  $Pe$ . This non-monotonic behavior arises because compaction influences dispersion mechanisms in multiple ways. As the porous medium becomes more compact, the influence of molecular diffusion weakens, while both mechanical dispersion and hold-up dispersion intensify. This study identifies new sources and behaviors of hold-up dispersion that were not detected by classical dispersion theory. Specifically, hold-up dispersion arises in regions with weak flow, distinguishing it from zero-velocity zones, such as dead-ends or the interiors of permeable grains, as described in classical dispersion theories. Moreover, the newly identified hold-up dispersion is active only within intermediate ranges of  $Pe$  ( $10^{-1} < Pe < 10^{-3}$ ). The interplay between reduced molecular diffusion and enhanced hold-up and mechanical dispersion, along with shifts in dominant dispersion mechanisms across varying  $Pe$ , results in multiple regimes in the  $\kappa - Pe$  curve. Additionally, the study demonstrates that compaction alters the pore structure by reducing pore size and changing the topology of the pore network. However, changes in topology counteract the effects of reduced pore size by limiting the increase in flow disorder. Thus, the influence of compaction on dispersion is closely linked to mechanical physics. Our study provides unique insights into the structural design and modulation of the dispersion coefficient of porous materials.

**KEYWORDS**

Compaction, Dispersion coefficient, Pore network model, Porous media

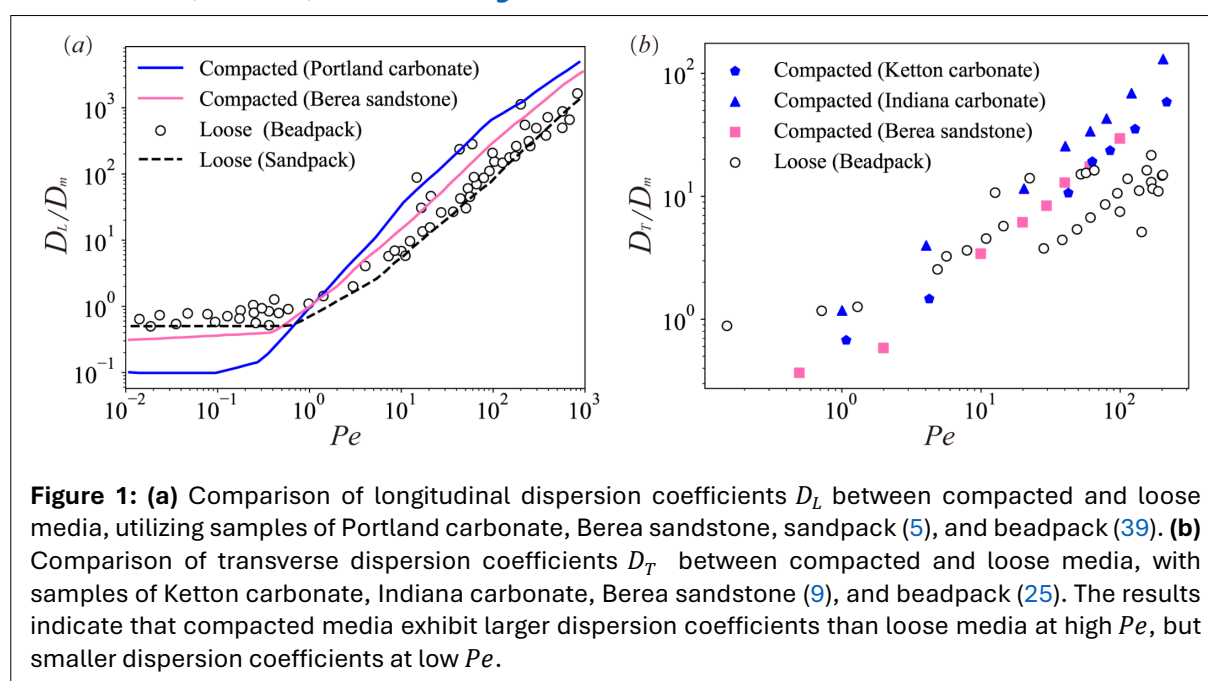


@2025 The Authors

This is an open access article published by InterPore under the terms of the Creative Commons Attribution-NonCommercial-NoDerivatives 4.0 International License (CC BY-NC-ND 4.0) (<https://creativecommons.org/licenses/by-nc-nd/4.0/>).

# 1. INTRODUCTION

Solute transport in porous media occurs in a wide range of physical, biological, and engineered systems, including ion transport in fuel cells (24), circulation in the human brain (16), and carbon dioxide geological sequestration (1, 7). The dispersion coefficient, a key parameter influencing solute transport, reflects the ability of porous media to attenuate concentration gradients (14). Porous media often experience compaction due to thermal stresses in geothermal systems (12), high-pressure injection in carbon sequestration (44), or geologic stresses at varying stratigraphic depths (23). This compaction alters pore structures—for instance, ground uplift by carbon dioxide injection in the In Salah formation (35, 46)—and can significantly influence flow dynamics and mass transfer. The effect of compaction on the dispersion coefficient of porous media has attracted extensive research interest. Most of the studies are conducted within the constraints of a low Péclet number  $Pe$ , which demonstrates that the dispersion coefficient decreases with the degree of compaction (20, 28). Nevertheless, certain investigations conducted at higher  $Pe$  have revealed an opposite trend, where the dispersion coefficient shows an increasing trend with the degree of compaction (11, 21, 36). Furthermore, several studies examining the dispersion coefficient in rocks have reported consistent findings. These studies illustrate a contrasting relationship between the dispersion coefficient and compaction degree across different values of the Péclet number (4, 5, 9, 17), as shown in Figure 1.



Despite widespread recognition of the intricate relationship between the dispersion coefficient and the degree of compaction, the underlying mechanisms remain poorly understood. Previous numerical studies on the effects of compaction on solute transport in porous media have predominantly relied on Darcy-scale models (8, 38, 43, 50), which fail to capture microscopic processes that critically influence flow and transport. On the other hand, although many existing studies (2, 6, 10, 41, 49) have examined the pore-scale complexity of porous structures, they neglect the evolution of pore geometry under compaction. However, precisely modeling pore structure evolution under compaction and direct simulation of solute transport over a wide range of  $Pe$  are constrained by computational limitations.

The discrete element method (DEM), which is a particle-based approach for simulating the dynamic behavior of granular materials under external forces (12, 40, 53), proved capable of capturing the evolution of the microstructure. In systems composed of spherical particles, DEM performs efficiently, whereas its efficiency decreases with non-spherical particles. Pore-scale modeling methods for flow and mass transfer through porous media are generally classified into two categories: direct numerical simulation (DNS) and pore network models (PNM). In DNS, the governing equations are solved directly on the exact pore structure. In contrast, PNM models these processes on a representative network with

idealized elements derived from the void space, which offers significantly higher computational efficiency than DNS. In recent years, PNM has seen growing use in the study of flow and transport phenomena within porous media (18, 29, 31, 32, 33), primarily due to its computational advantage over DNS.

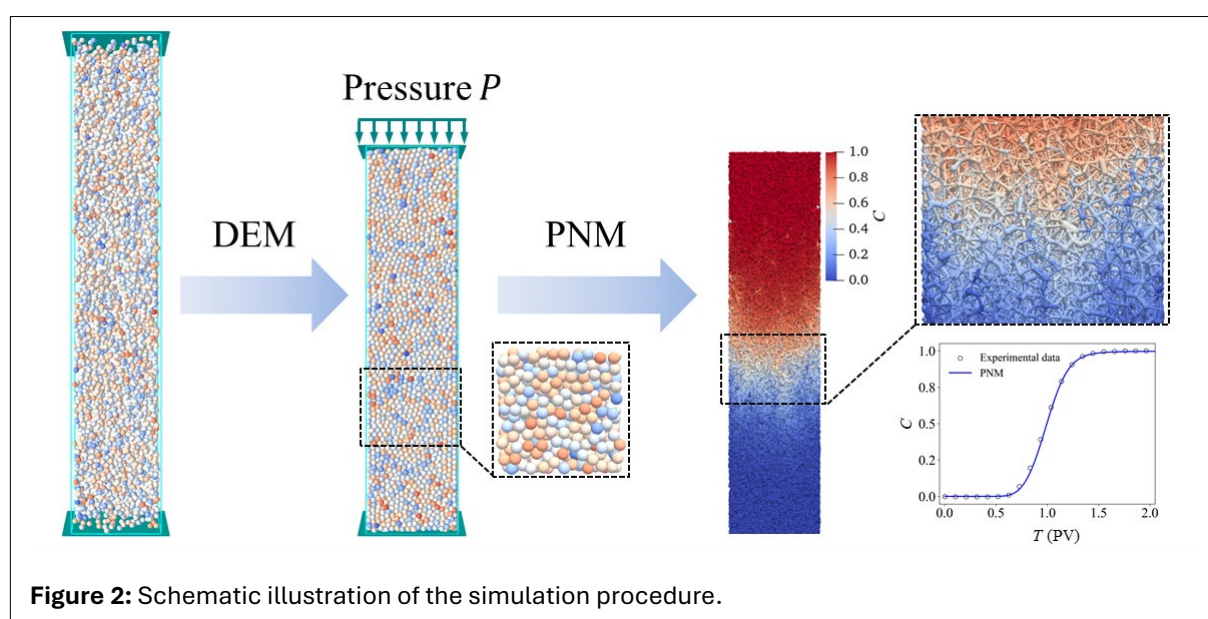
This study investigates the impact of compaction on the dispersion coefficient of granular media using a numerical framework that combines DEM and PNM. The framework captures the essential physical processes, including the evolution of pore geometry under compaction and pore-scale transport, while maintaining a practical computational cost for comprehensive investigations across a wide range of compaction degrees and Péclet numbers, and thereby overcoming the limitations of previous research. Within the framework, DEM is employed to generate sphere packs at varying compaction levels. The pore network is then extracted from the generated structure, and simulations of fluid flow and solute transport are conducted to determine the dispersion coefficient. The relationship between the dispersion coefficient and the degree of compaction over a broad range of Péclet numbers, along with the underlying mechanisms, is analyzed. This study offers valuable insights into the structural design and regulation of hydrodynamic dispersion in porous materials.

This paper is structured as follows. Section 2 introduces the DEM-PNM framework and describes the setup of the numerical simulations. Section 3 presents the numerical results, highlighting the non-monotonic relationship between the dispersion coefficient and compaction, along with an explanation of the underlying mechanisms. Finally, Section 4 concludes the paper by summarizing the key findings.

## 2. METHODS

We combine DEM and PNM to investigate the impact of compaction on the dispersion coefficient of sphere packs. It is assumed that the time scale of fluid flow is much shorter than that of structural deformation; thus, the flow remains in a steady state. Based on this assumption, structural deformation and solute transport are treated as independent processes, which significantly enhances the computational efficiency of the framework. However, this assumption also imposes limitations, as it prevents the study from capturing transient solute transport coupled with structural deformation.

The simulation consists of two steps, as illustrated in Figure 2. First, DEM simulations track the movement of individual spheres, and determine the pore structure once the sphere assembly reaches a steady state under a specific pressure load  $P$ . The second step involves extracting the pore network from the resulting pore structure, followed by PNM simulations of solute transport to obtain the dispersion coefficient for the various Péclet numbers ( $Pe$ ).



Discrete element method simulations are executed using the open-source software Yade (52), with the contact model and the integral model serving as two crucial components. To speed up computation, the linear-spring-damping model (13) is employed to calculate contact forces between spheres and an explicit integration algorithm is utilized to update the positions of the spheres. The validity of the DEM algorithm has been confirmed by experimental data on the permeability-porosity relationship (51), as shown in **Figure S1** in the **Supplementary Material** (available online). In the simulations, the spheres are assigned a Young's modulus  $E$  of 2.5 GPa and a Poisson's ratio of 0.33. These parameters are chosen in accordance with the properties typically observed in sedimentary rocks (19, 34). A total of 40,000 spheres are randomly distributed within a confined box, enclosed by rigid walls on all four sides and at the bottom. The number of spheres is limited by the computational cost of the DEM; however, when feasible, increasing their number enables the model to more accurately approximate the representative elementary volume (REV). Pressure is exerted from the top, compressing the spheres and causing them to move downward. The spheres eventually reach a stable configuration for the specific pressure load  $P$ , where  $P$  spans a range from the pressure load  $P_0 = 5$  MPa to the maximum pressure load  $P_{\max} = 70$  MPa. The overburden stress gradient in the formation is approximately 0.026 MPa/m (34); thus, the applied pressure range corresponds to formation depths of about 190~2700 m, which are typical in oil recovery and CO<sub>2</sub> sequestration operations. Interactions between spheres upon contact result in elastic deformation, altering their original spherical shape.

The pore network simulations were conducted using our house-hold program. The pore network is extracted from the pore structure generated by the aforementioned DEM simulation, using a pore-throat segmentation algorithm based on local resistance equivalence (32). For steady-state, single-phase incompressible fluid flow, the flow field across the pore network is determined from the mass conservation for each pore. For pore  $i$ , the mass conservation equation is expressed as (Eq. 1):

$$\sum_j q_{ij} = 0 \quad (1)$$

where  $q_{ij}$  represents the flow rate between pore  $i$  and its neighboring pore  $j$ , calculated by (Eq. 2):

$$q_{ij} = g_{ij}(P_i - P_j) \quad (2)$$

Here,  $P_i$  and  $P_j$  are pressures in pores  $i$  and  $j$ , respectively, and  $g_{ij}$  denotes the hydraulic conductance between them. This conductance is determined as the harmonic mean of the conductance of each element (Eq. 3):

$$g_{ij} = \frac{1}{\frac{1}{g_i} + \frac{1}{g_t} + \frac{1}{g_j}} \quad (3)$$

where  $g_i$ ,  $g_j$ , and  $g_t$  represent conductance of pores  $i$  and  $j$  and the interconnecting throat  $t$ , respectively. The hydraulic conductance of an individual network element is calculated as (Eq. 4):

$$g = \frac{kGA^2}{\mu l} \quad (4)$$

where  $\mu$  is the fluid viscosity,  $l$  is the conduit length,  $A$  is the cross-sectional area,  $G$  is the shape factor that distinguishes the cross-sectional shape of the network elements, and  $k$  is a coefficient dependent on the cross-sectional shape. The shape factor is defined as  $G = R^2/4A$  where  $R$  denotes the inscribed radius of the element. In this model, network elements with triangular ( $0 < G \leq \frac{\sqrt{3}}{36}$ ), square ( $\frac{\sqrt{3}}{36} < G < \frac{1}{4\pi}$ ), and circular ( $G \geq \frac{1}{4\pi}$ ) cross-sectional shapes are considered, with corresponding values of  $k$  being 0.6, 0.5623, and 0.5 (37), respectively.

The solute is transported through both advection and diffusion, and the evolution of the concentration field is described by mass conservation within each pore and throat. For the control volume of pore  $i$ , the mass conservation is as follows (Eq. 5):

$$V_i \frac{dC_i}{dt} = \sum_{\text{in}} q_{ij} \cdot C_{ij} - \sum_{\text{out}} q_{ij} \cdot C_i + \sum_j \frac{C_{ij} - C_i}{\frac{l_i}{D_{\text{sd},i}A_i} + \frac{0.5l_{ij}}{D_{\text{sd},ij}A_{ij}}} \quad (5)$$

The term on the left-hand side represents the net mass accumulation within the control volume, while the terms on the right-hand side correspond to mass exchange due to advective inflow, advective outflow, and diffusive mass exchange, respectively. Here,  $C_i$ ,  $V_i$ ,  $l_i$ , and  $A_i$  represent the concentration, the volume, the diffusive conduit length, and the cross-sectional area of pore  $i$ , respectively. The corresponding quantities for throat  $ij$  are denoted with a similar notation but with the subscript  $i$  changed to  $ij$ .  $D_{\text{sd}}$  denotes the pore-scale shear dispersion coefficient, which captures the effect of parabolic velocity profiles on mass transfer within individual pores or throats, i.e., shear dispersion.  $D_{\text{sd}}$  is calculated as follows (30; Eq. 6):

$$\frac{D_{\text{sd}}/D_m - 1}{\kappa Pe^2} = 1 - \exp\left(-\beta \frac{D_m}{R^2} t\right) \quad (6)$$

where  $\beta$  is a coefficient dependent on the shape of the conduit cross-sections, with values of 15, 10.8, and 4.8 for conduits with circular, square, and triangular cross-sections. For the control volume of throat  $ij$ , the mass conservation is expressed as follows (Eq. 7):

$$V_{ij} \frac{dC_{ij}}{dt} = q_{ij}(C_{\text{in}} - C_{\text{out}}) + \frac{C_i - C_{ij}}{\frac{l_i}{D_{\text{sd},i}A_i} + \frac{0.5l_{ij}}{D_{\text{sd},ij}A_{ij}}} + \frac{C_j - C_{ij}}{\frac{l_j}{D_{\text{sd},j}A_j} + \frac{0.5l_{ij}}{D_{\text{sd},ij}A_{ij}}} \quad (7)$$

where  $C_{\text{in}}$  and  $C_{\text{out}}$  are inflow and outflow concentrations, respectively. The implicit scheme is employed to solve the concentration field.

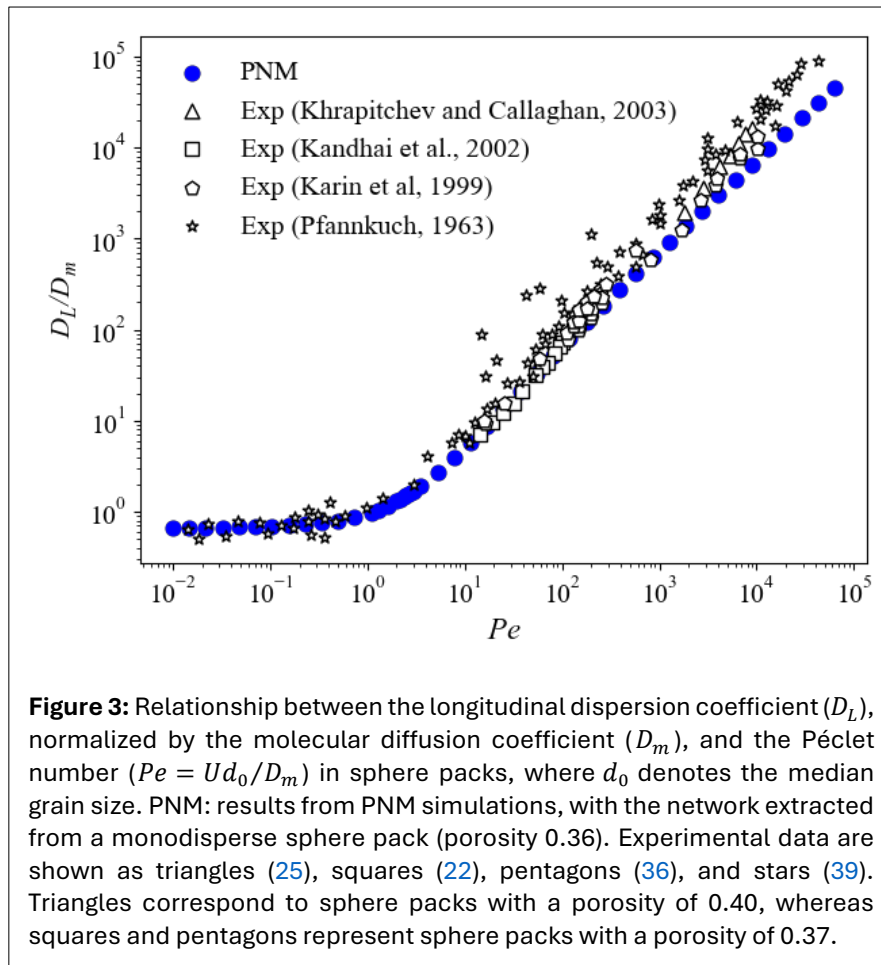
In the flow simulation, Dirichlet boundary conditions are applied to the pressure field at both the inlet and outlet, with the pressure drop adjusted to achieve specific Péclet numbers. For solute transport simulation, a constant concentration is maintained at the inlet, while a zero concentration gradient is imposed at the outlet. The dispersion coefficient is determined by fitting the breakthrough curve at the outlet to the analytical solution as shown (27; Eq. 8):

$$\begin{aligned} C(x, T) = & 0.5\text{erfc}\left(\frac{x - UT}{2\sqrt{D_L T}}\right) + 0.5\exp\left(\frac{Ux}{D_L}\right)\text{erfc}\left(\frac{x + UT}{2\sqrt{D_L T}}\right) \\ & + 0.5\left(2 + \frac{U(2L - x)}{D_L} + \frac{U^2 T}{D_L}\right)\exp\left(\frac{UL}{D_L}\right)\text{erfc}\left(\frac{(2L - x + UT)}{2\sqrt{D_L T}}\right) \\ & - \sqrt{\frac{U^2 T}{\pi D_L}}\exp\left(\frac{UL}{D_L} - \frac{(2L - x + UT)^2}{4D_L T}\right) \end{aligned} \quad (8)$$

where  $D_L$  is the dispersion coefficient,  $U$  is the mean velocity,  $T$  is the injection time,  $L$  is the longitudinal length of the domain,  $x$  is the observation location, and  $C$  is the concentration.

The reliability and accuracy of our PNM algorithm have been proved through rigorous validation against DNS solutions and experimental data, demonstrating relative errors of less than 6% in predicted permeability (32) and breakthrough curve (30), as shown in **Figures S2** and **S3** in the **Supplementary Material** (available online), respectively. This study further assesses its reliability and accuracy by comparing the predicted relationship between the normalized longitudinal dispersion coefficient and the Péclet number in sphere packs with experimental data. The results, presented in **Figure 3**, demonstrate that the PNM predictions are in good agreement with the experimental data.





### 3. RESULTS AND DISCUSSION

This study investigates four distinct groups of sphere packs, characterized by a normal distribution of grain size  $d$ , as illustrated in Figure 4. Each group has the same median diameter,  $d_0 = 140 \mu\text{m}$ , but varies in standard deviations,  $\sigma = 0, 0.025 d_0, 0.05 d_0$ , and  $0.1 d_0$ , respectively. To minimize the influence of domain size on simulation results, a subdomain measuring  $13 d_0 \times 13 d_0 \times 95 d_0$  is extracted from the pore structure for subsequent flow and mass transfer simulations. The Péclet number is defined as  $Pe = Ud_0/D_m$ , where  $U$  represents the average velocity, calculated as the Darcy velocity divided by porosity, and  $D_m$  is the molecular diffusion coefficient, set at  $4.6 \times 10^{-10} \text{ m}^2/\text{s}$ .

To present the results more clearly, the dispersion coefficient is normalized by that under the initial pressure load  $P_0$ . Figure 5a shows the variation of the normalized dispersion coefficient,  $D_L^P/D_L^{P_0}$ , with the pressure load  $P$  for different values of  $Pe$ , revealing a non-monotonic relationship. Specifically, at low  $Pe$  values, the dispersion coefficient decreases with increasing pressure load, while at high  $Pe$  values, the trend reverses. This observation aligns with previous experimental findings (11, 20, 21, 28, 36).

The variation in dispersion coefficients is defined as  $\kappa = D_L^{P_{\max}}/D_L^{P_0} - 1$ , where  $D_L^{P_0}$  and  $D_L^{P_{\max}}$  are the dispersion coefficients under the initial pressure load  $P_0$  and the maximum pressure load  $P_{\max}$ , respectively. The maximum values of  $\kappa$  are 0.39, 0.44, 0.47, and 0.48, corresponding to sphere packs with  $\sigma/d_0 = 0, 0.025, 0.05$ , and  $0.1$ , respectively. These results align with the experimental data (36), which indicated a  $\kappa$  of approximately 1 for sphere packs with  $\sigma/d_0 = 0.19$ , associated with a decrease in porosity from 36.8% to 23.7%. The variation of  $\kappa$  with  $Pe$  reveals three distinct regimes, as illustrated in Figure 5b. In Regime I ( $Pe < 10^{-1}$ ),  $\kappa$  remains negative and shows consistent independence from  $Pe$ . In Regime II ( $10^{-1} < Pe < 10^3$ ),  $\kappa$  transitions from negative to positive, peaking around  $Pe$  of 30 before stabilizing at a positive plateau. In Regime III ( $Pe > 10^3$ ),  $\kappa$  stays positive and invariant with  $Pe$ . All four groups of sphere packs exhibit a similar relationship between the dispersion coefficient and the pressure

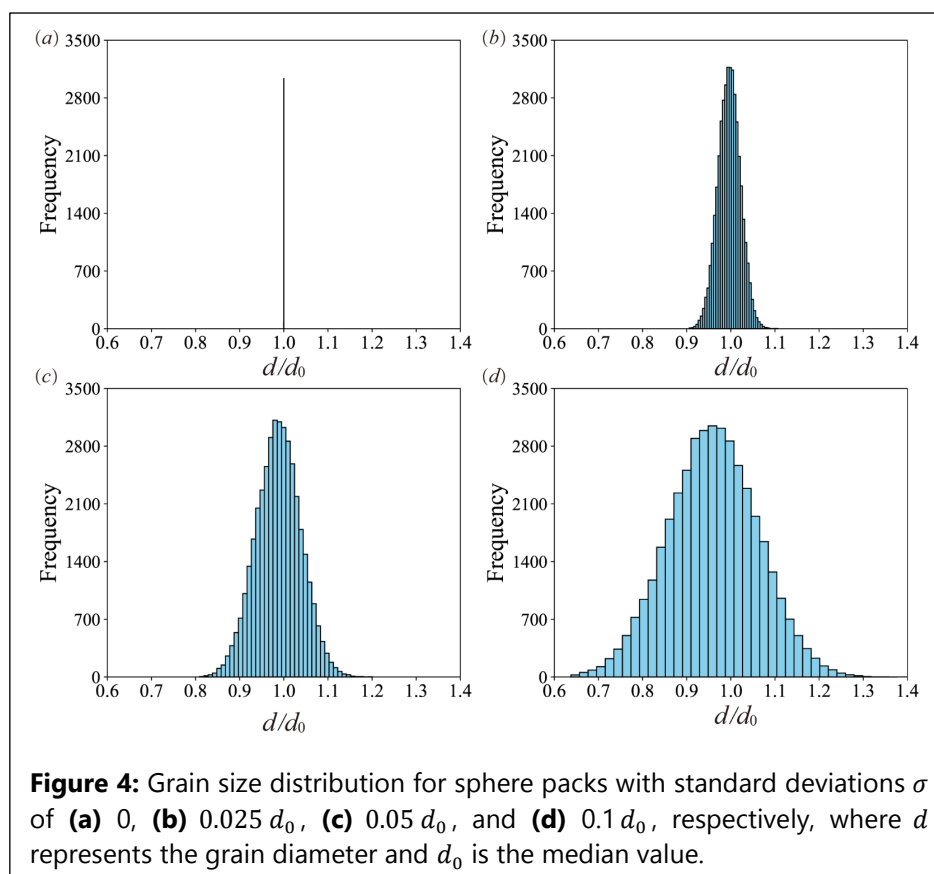


**Figure 4:** Grain size distribution for sphere packs with standard deviations  $\sigma$  of (a) 0, (b)  $0.025 d_0$ , (c)  $0.05 d_0$ , and (d)  $0.1 d_0$ , respectively, where  $d$  represents the grain diameter and  $d_0$  is the median value.

load. For brevity, we focus on the results and analysis for monodisperse sphere packs ( $\sigma = 0$ ), while the findings for polydisperse sphere packs ( $\sigma = 0.025 d_0, 0.05 d_0$ , and  $0.1 d_0$ ) will be summarized at the end of this section. Throughout the discussion, “sphere packs” will refer to monodisperse packs unless otherwise specified.

The diverse regimes of  $\kappa$  as it varies with  $Pe$  can be attributed to several underlying physical mechanisms that contribute to dispersion under laminar flow conditions: molecular diffusion, shear dispersion, hold-up dispersion, and mechanical dispersion (26). Molecular diffusion arises from the random thermal motion of solute molecules or particles. Shear dispersion, also known as boundary-layer dispersion, results from non-uniform velocity profiles within pores or throats. Classical dispersion theories (26, 48)

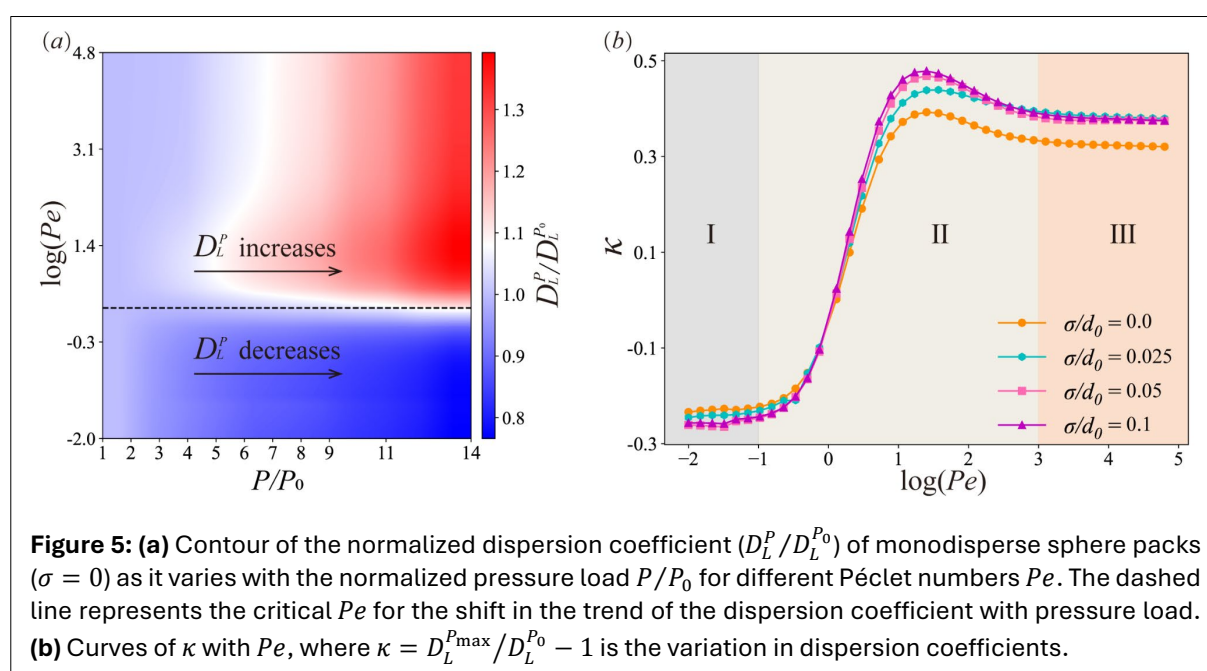
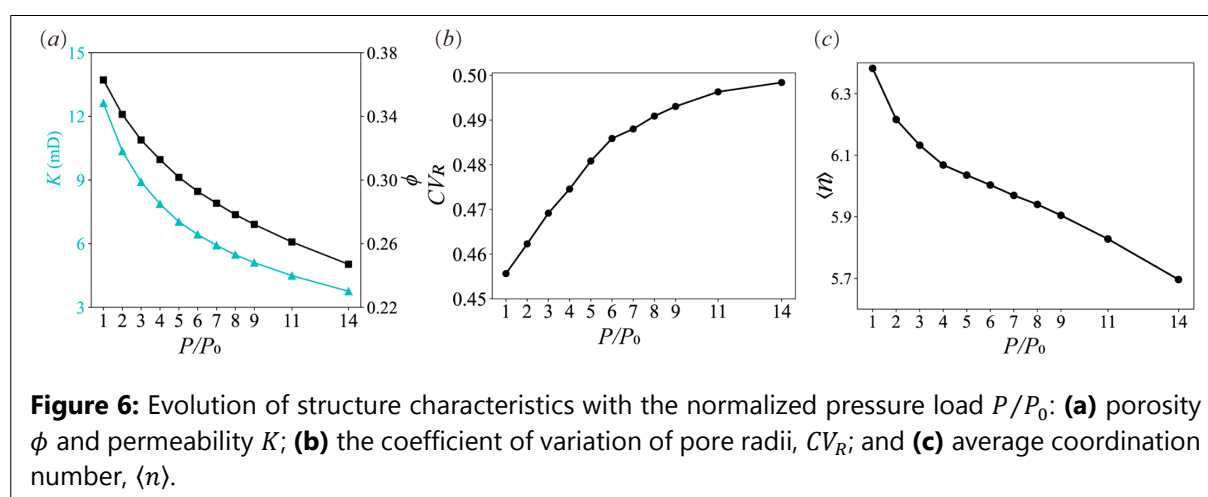


**Figure 5:** (a) Contour of the normalized dispersion coefficient ( $D_L^P/D_L^{P_0}$ ) of monodisperse sphere packs ( $\sigma = 0$ ) as it varies with the normalized pressure load  $P/P_0$  for different Péclet numbers  $Pe$ . The dashed line represents the critical  $Pe$  for the shift in the trend of the dispersion coefficient with pressure load. (b) Curves of  $\kappa$  with  $Pe$ , where  $\kappa = D_L^{P_{\max}}/D_L^{P_0} - 1$  is the variation in dispersion coefficients.

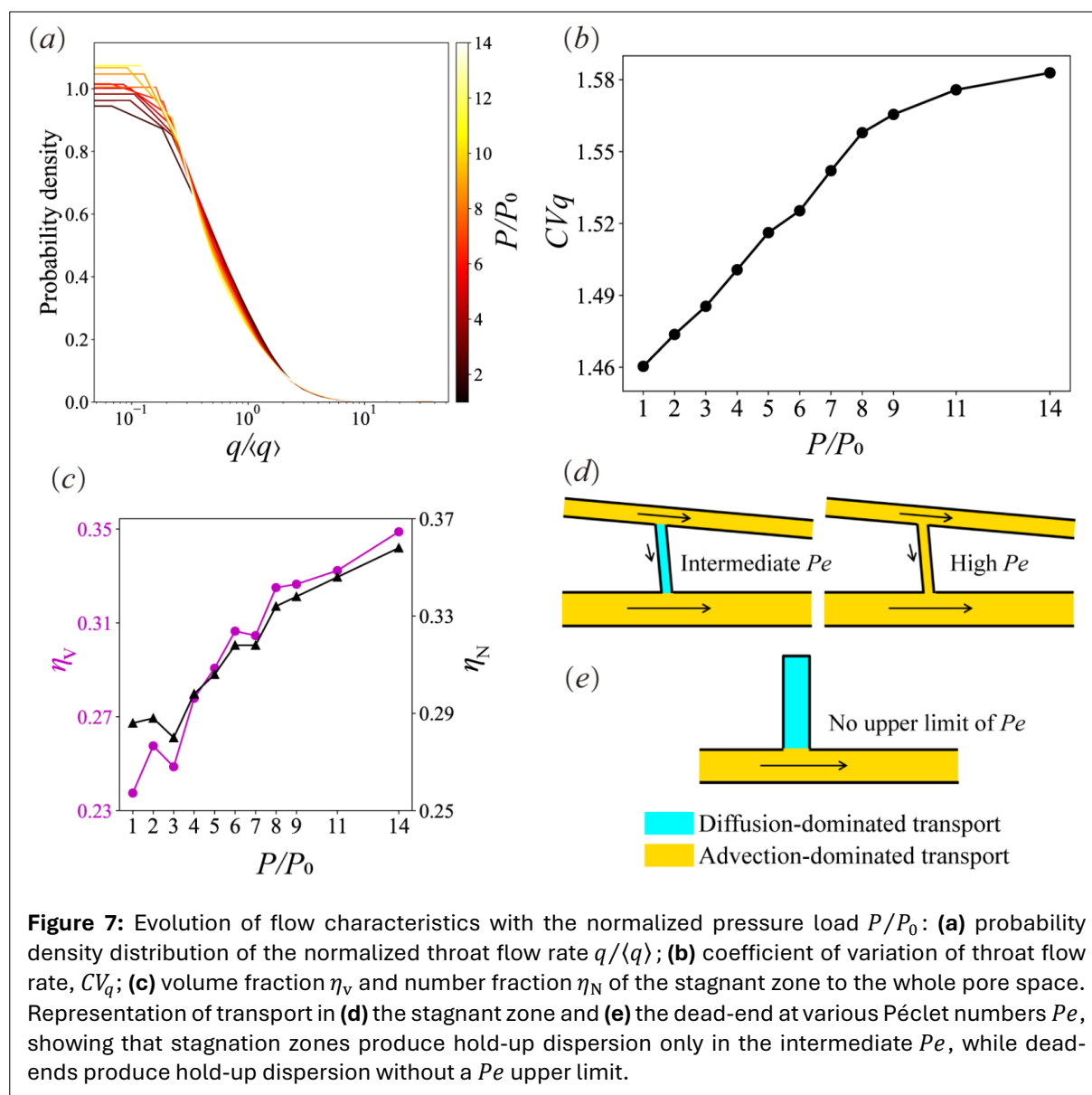
suggest that hold-up dispersion occurs due to the retention of solute species in regions of zero velocity, such as the interiors of permeable solid grains or dead-ends, where escape is only possible through molecular diffusion. However, this study shows that low-velocity regions in porous media, where flow exists but is weak, also contribute to hold-up dispersion. Mechanical dispersion, on the other hand, results from the repeated splitting and merging of flow passages at pore junctions. At low  $Pe$  values, advection has a minimal effect, and molecular diffusion is the dominant mechanism. As  $Pe$  increases, advection exerts an increasingly important influence on dispersion. At high  $Pe$ , mechanical dispersion becomes the primary mechanism. In the intermediate range of  $Pe$ , all four mechanisms—molecular diffusion, shear dispersion, hold-up dispersion, and mechanical dispersion—operate together, influencing the overall dispersion.

To evaluate the effects of increased compaction on dispersion mechanisms, the first step is to examine changes in the pore structure and the resulting alterations in flow within the porous medium. As the pressure load rises from the pressure load,  $P_0$ , to the maximum pressure load,  $P_{\max}$ , the pore structure of the sphere packs becomes tighter. **Figure 6a** shows a decrease in porosity,  $\phi$ , from 0.362 to 0.247, accompanied by a reduction in permeability,  $K$ , from 12.6 mD to 3.8 mD. The coefficient of variation of pore radii, defined as  $CV_R = \sigma_R / \langle R \rangle$ , where  $\sigma_R$  and  $\langle R \rangle$  represent the standard deviation and mean of the pore radii, respectively, increases with increasing pressure loads (see **Fig. 6b**). This trend indicates intensified heterogeneity in the pore structure. Increased compaction also results in a decrease in the coordination number of pores, as illustrated in **Figure 6c**, leading to reduced connectivity within the pore network. The disorder of flow in the porous medium is further characterized by the coefficient of variation of throat flow rates,  $CV_q = \sigma_q / \langle q \rangle$ , where  $\sigma_q$  and  $\langle q \rangle$  denote the standard deviation and mean of throat flow rates, respectively.



The number and volume ratios of dead-end pores consistently remain below 0.3% and 0.1%, respectively, indicating a negligible impact. This aligns with the findings of Koch and Brady (26), who reported negligible zero-velocity regions within sphere packs. Nevertheless, stagnant zones characterized by weak flow are prevalent within the sphere packs. These stagnant zones are identified based on the following procedure. First, transit times  $V/q$  through network elements (pores and throats) are sorted in descending order, where  $V$  and  $q$  represent the volume and flow rate of these elements, respectively. The sorted network elements are labeled from 1 to  $N_0$  based on their ranking order, where  $N_0$  denotes the total number of network elements. Following this, elements are removed from the network, starting with those having the smallest labels. The number of elements removed is represented by  $N$ , indicating the removal of all elements with labels less than  $N$ . Subsequently, the permeability  $K$  of the modified pore network is determined. Next, the derivative  $\frac{\Delta(K/K_0)}{\Delta(N/N_0)}$  of the normalized permeability  $K/K_0$  to the removal ratio  $N/N_0$  is calculated, where  $K_0$  denotes the permeability of the original network. The removal number when  $\frac{\Delta(K/K_0)}{\Delta(N/N_0)} = -1$  is denoted as  $N_c$ . The stagnant zone is defined as the sorted network elements with labels  $N < N_c$ . As shown in **Figure 7c**, the volume and number fractions of stagnant zones, denoted as  $\eta_v$  and  $\eta_N$ , respectively, increase significantly with higher pressure loads, reaching up to 35%.





Previous studies have recognized the existence of these low-velocity regions in porous media and suggested their potential impact on dispersion (42, 45, 54).

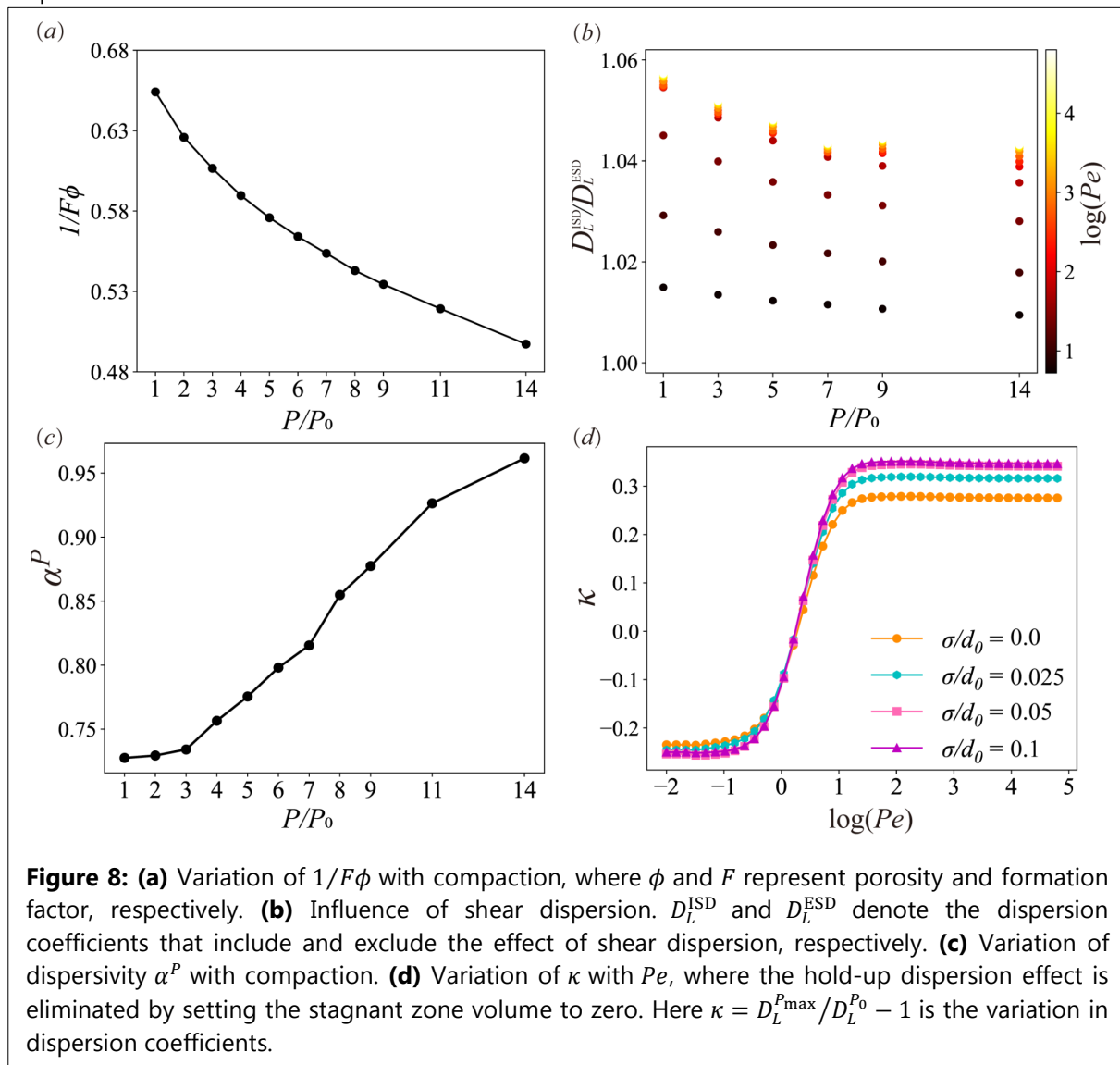
We further demonstrate that stagnant zones, similar to dead-end pores, induce a retention effect on solute species, leading to hold-up dispersion. Flow occurs within stagnant zones, albeit at a significantly lower rate than the average flow through the porous medium. In the intermediate  $Pe$  range ( $10^{-1} < Pe < 10^3$ ), advection dominates solute transport outside stagnant zones, while molecular diffusion dominates transport within them. Similar to zero-velocity regions, the stagnant zone creates simultaneous advection- and diffusion-dominated transport (26), as shown in Figure 7d,e, leading to hold-up dispersion. However, as  $Pe$  increases, solute transport within the stagnant zone becomes dominated by advection, leading to the disappearance of the hold-up effect. Thus, hold-up dispersion caused by stagnant zones is confined to the intermediate range of  $Pe$  ( $10^{-1} < Pe < 10^3$ ). It is important to note that stagnant zones differ from zero-velocity regions. In zero-velocity regions, solute transport is consistently dominated by molecular diffusion, regardless of  $Pe$ , resulting in hold-up dispersion without an upper  $Pe$  limit.

In regime I ( $Pe < 10^{-1}$ ), molecular diffusion emerges as the primary mechanism governing dispersion, with the dispersion coefficient  $D_L^P$  solely dependent on the nature of the pore structure and independent of  $Pe$ . The relationship can be expressed as  $D_L^P/D_m = 1/F\phi$ , where  $F$  represents the formation factor. The formation factor quantifies the normalized electrical resistance of the pore structure and is

analogous to the absolute permeability of porous media. Our previous work (30) provides a detailed explanation of how the pore network model calculates the formation coefficient. As shown in Figure 8a, the magnitude of  $1/F\phi$  decreases as pressure load increases, which accounts for the observed negative value of  $\kappa$ .

In regime III ( $Pe > 10^3$ ), mechanical dispersion predominates, resulting in a linear relationship between the dispersion coefficient  $D_L^P$  and the Péclet number  $Pe$ , expressed as  $D_L^P = \alpha^P Pe$  (3, 47). Here,  $\alpha^P$  denotes the dispersivity of the sphere pack, which depends on the characteristics of porous media flow; specifically, increased disorder in the flow corresponds to a higher value of  $\alpha^P$ . Thus, we obtain  $\kappa = \alpha^{P_{\max}}/\alpha^{P_0} - 1$ , where  $\alpha^{P_0}$  and  $\alpha^{P_{\max}}$  denote the dispersivity of the sphere pack at the initial pressure load  $P_0$  and the maximum pressure load  $P_{\max}$ , respectively. The influence of  $Pe$  is canceled out, indicating that  $\kappa$  is independent of  $Pe$ . The heterogeneity of the pore structure, quantified by  $CV_R$ , increases with the rising pressure load (Fig. 6b). Consequently, as illustrated in Figure 7b, the flow disorder, represented by the coefficient of variation of throat flow rates  $CV_q$ , intensifies. This results in an increase in dispersivity (10, 48), as depicted in Figure 8c. Therefore,  $\kappa$  maintains a positive plateau in this regime.

In regime II ( $10^{-1} < Pe < 10^3$ ), the Péclet number spans a wide range, indicating that both advection and diffusion can influence the dispersion coefficient. This regime is marked by the interplay of various dispersion mechanisms, including molecular diffusion, shear dispersion, hold-up dispersion, and mechanical dispersion. It has been revealed that increased compaction weakens molecular diffusion but enhances mechanical dispersion. However, the impact of compaction on shear dispersion and hold-up dispersion remains unclear.

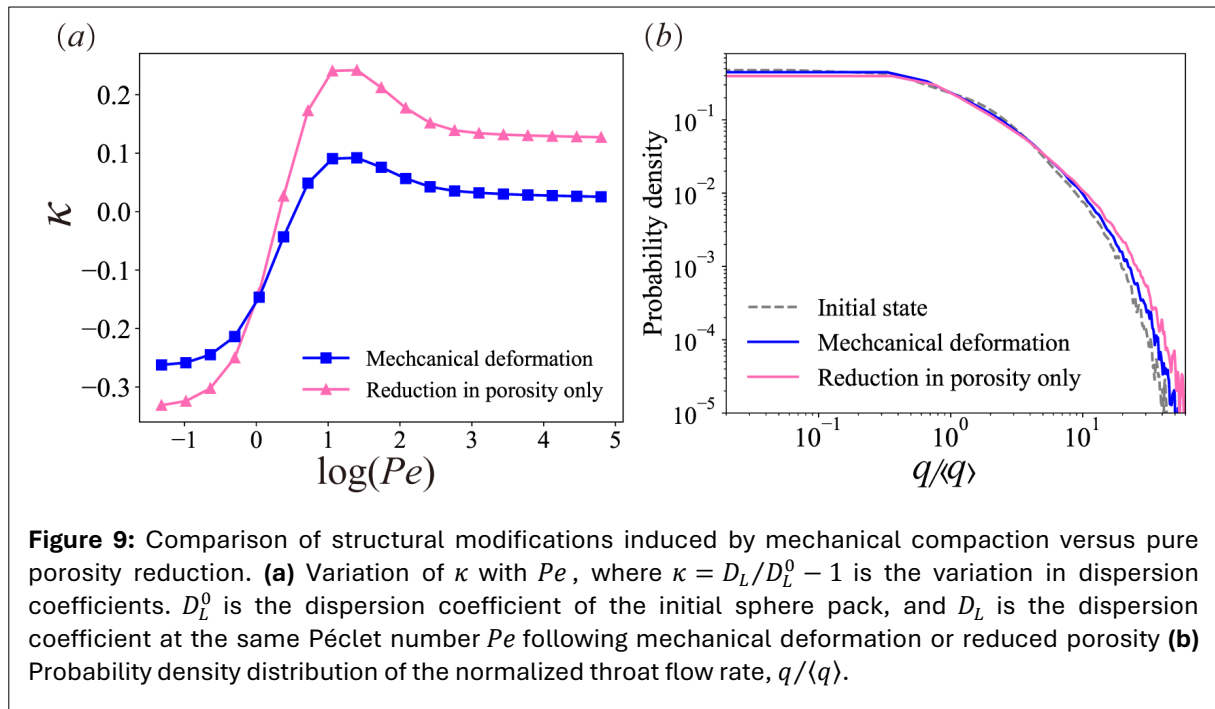


We assess the role of shear dispersion by comparing global dispersion coefficients that either include or exclude its effects. In the network model, shear dispersion is incorporated using pore-scale shear dispersion coefficients  $D_{sd}$  to calculate diffusive mass transfer fluxes, as described in [Equations 5 and 7](#). Conversely, replacing  $D_{sd}$  with the molecular diffusion coefficient  $D_m$  ignores the effect of parabolic velocity profiles, deactivating the shear dispersion effect. This substitution does not alter porous media flow, leaving mechanical and stagnant dispersion unchanged. [Figure 8b](#) indicates that shear dispersion has a minimal effect on the overall dispersion coefficient, accounting for less than 6%. This result is consistent with previous findings ([30](#)), showing that shear dispersion contributes negligibly to overall mass transfer in highly disordered pore structures.

Classical dispersion theories ([26, 48](#)) propose that hold-up dispersion arises from the retention of solutes in dead-ends and within permeable grains, where solute transport is primarily governed by molecular diffusion. Outside these regions, solute transport is dominated by advection. The coexistence of advection- and diffusion-dominated zones gives rise to hold-up dispersion. However, in this study, the negligible presence of dead-ends and the impermeable grains raise questions about the existence of hold-up dispersion in the structures examined. If hold-up dispersion were absent, and given the minimal impact of shear dispersion, the dispersion within regime II would shift from being dominated by weakened molecular diffusion to enhanced mechanical dispersion as  $Pe$  increases. Since the effects of both molecular diffusion and mechanical dispersion on  $\kappa$  are independent of  $Pe$ , we would expect  $\kappa$  to transition smoothly from negative to positive values as  $Pe$  rises. However, this predicted smooth transition contradicts the peak observed in the  $\kappa - Pe$  curve, suggesting the involvement of other mechanisms that intensifies with increasing pressure load and acts only near the peak. We demonstrate that the observed peak in the  $\kappa - Pe$  curve is attributed to hold-up dispersion arising from stagnant regions. Within an intermediate range of  $Pe$  ( $10^{-1} < Pe < 10^3$ ), the flow inside stagnant regions is sufficiently slow that solute transport is governed by molecular diffusion, whereas advection dominates outside these regions. This coexistence of advection- and diffusion-dominated zones gives rise to hold-up dispersion. As  $Pe$  increases further, the flow within stagnant zones intensifies, and transport there becomes advection dominated; consequently, only advection-dominated zones remain in the pore space, and hold-up dispersion vanishes. In other words, the hold-up dispersion induced by stagnant regions only works within an intermediate range of  $Pe$  ( $10^{-1} < Pe < 10^3$ ). This explanation is also supported by a recent theoretical model based on the Continuous Time Random Walk (CTRW) framework ([42](#)). As the pressure load increases, the fraction of stagnant zones grows, as shown in [Figure 7c](#), leading to enhanced hold-up dispersion. These features account for the observed peak in the  $\kappa - Pe$  curve. By setting the volumes of the pores and throats within stagnant zones to zero while maintaining other parameters consistent with the base case, the effect of hold-up dispersion is turned off. The removal of hold-up dispersion, as illustrated in [Figure 8d](#), leads to the disappearance of the peak in the  $\kappa - Pe$  curve, further validating our perspective.

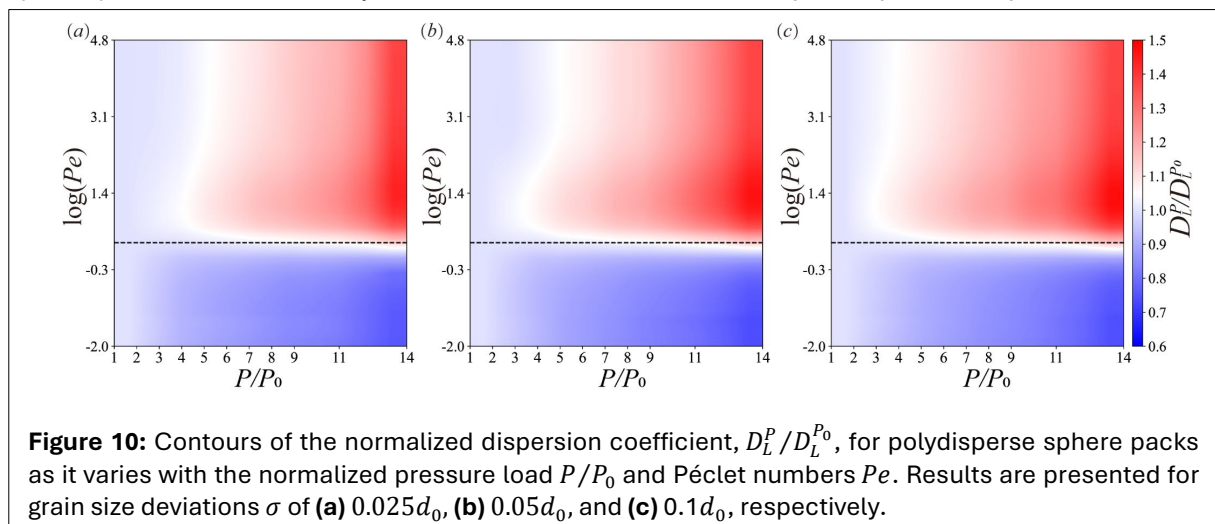
In conclusion, the mechanisms that essentially play roles in regime II are molecular diffusion, hold-up dispersion, and mechanical dispersion. As the pressure load increases, the weakening of molecular diffusion competes with the enhancement of hold-up dispersion and mechanical dispersion. On the other hand, as  $Pe$  increases, advection increasingly influences dispersion, resulting in a transition from a state primarily governed by molecular diffusion to one where hold-up and mechanical dispersions jointly dominate. The shift in the dominance of dispersion mechanisms leads to a change in  $\kappa$  from a negative to a positive value, i.e., the dependence between the dispersion coefficient and the pressure load changes from negative to positive.  $\kappa$  reaches its peak around  $Pe = 30$  and subsequently undergoes a decline. This trend is explained by the fact that hold-up dispersion induced by stagnant zone diminishes at high  $Pe$ , leading to a shift in the increase of the dispersion coefficient from being driven by both hold-up and mechanical dispersions to one driven solely by mechanical dispersion.

We further investigate how compaction affects pore structure and its influence on flow and dispersion. Compaction not only reduces pore size but also alters the topology of the pore network (see [Fig. 6c](#)), leading to decreased porosity and changes in flow pathways. To assess the effects of these structural changes, we compare dispersion coefficients under structural modifications induced by two distinct methods. The first method involves mechanically deforming the initial sphere pack by applying a



pressure load, while the second method uniformly increases the sphere size within the initial pack to achieve the same porosity as mechanical compaction. The initial porosity is 0.45, while both mechanical compaction and increased sphere size reduce the porosity to 0.3. The change in the dispersion coefficient is defined as  $\kappa = D_L/D_L^0 - 1$ , where  $D_L^0$  is the dispersion coefficient of the initial sphere pack and  $D_L$  is the dispersion coefficient at the same Péclet number  $Pe$  following mechanical deformation or reduced porosity. The results illustrated in **Figure 9a** reveal that a reduction in porosity alone leads to a more substantial change in the dispersion coefficient than mechanical deformation. This occurs because the reduction in porosity has a greater impact on flow within porous media than mechanical deformation, as further illustrated in **Figure 9b**. More quantitatively, the coefficients of variation of throat flow rates,  $CV_q$  for the sphere packs in their initial state, after mechanical deformation, and after only porosity reduction are 1.55, 1.59, and 1.68, respectively. These values indicate that porosity reduction alone creates a structure with greater flow disorder compared to mechanical deformation. Furthermore, the findings suggest that changes in pore network topology can mitigate the effects of reduced pore size by limiting the increase in flow disorder. In other words, the influence of compaction on dispersion involves mechanical physics, highlighting the necessity of DEM simulations in this study, rather than relying solely on the reduction of porosity in the porous media.

**Figure 10** presents the normalized dispersion coefficient  $D_L^P/D_L^{P_0}$  for three groups of polydisperse sphere packs, characterized by standard deviations of  $\sigma = 0.025d_0$ ,  $0.05d_0$ , and  $0.1d_0$ , as it varies with



the pressure load across various  $Pe$ . The results indicate a trend consistent with those found in monodisperse sphere packs ( $\sigma = 0$ ), suggesting that the conclusions drawn from monodisperse packs can be extended to polydisperse cases. In this study, the standard deviation  $\sigma$  is capped at  $0.1 d_0$  due to the computational demands of DEM simulations, as larger deviations would require a greater number of spheres. However, we anticipate that the conclusions are generalizable to sphere packs with a broader range of grain size distributions.

## 4. CONCLUSIONS

We investigate the impact of compaction on the longitudinal dispersion coefficient of porous materials using a DEM-PNM numerical framework. This work has yielded the following innovative findings: **1)** the variation of the dispersion coefficient, denoted as  $\kappa$ , exhibits a non-monotonic relationship with increasing compaction, characterized by three distinct regimes across different Péclet numbers  $Pe$ . Specifically, as the degree of compaction increases (porosity decreases from 0.362 to 0.247), the dispersion coefficient may decrease by up to 20% or increase by nearly 50% in magnitude, depending on  $Pe$ . Statistical analysis of pore structures and flow fields reveals that compaction influences dispersion mechanisms in multiple ways. As the porous medium becomes denser under higher pressure, the impact of molecular diffusion, which dominates at low  $Pe$  ( $Pe < 10^{-1}$ ), weakens. In contrast, increased compaction enhances pore structure heterogeneity, leading to greater disorder and a higher proportion (increase from 23% to 35%) of stagnant regions within the flow. These changes further strengthen mechanical dispersion and hold-up dispersion. Mechanical dispersion is active across both moderate ( $10^{-1} < Pe < 10^3$ ) and high  $Pe$  ( $Pe > 10^3$ ) values, whereas hold-up dispersion predominantly occurs at intermediate  $Pe$  ( $10^{-1} < Pe < 10^3$ ) values. **2)** We reveal that hold-up dispersion arises from stagnant regions with weak flow, fundamentally different from zero-velocity regions (such as dead-ends or the interiors of permeable grains) described in classical dispersion theories (26, 48). The interplay between reduced molecular diffusion and enhanced hold-up and mechanical dispersion, along with shifts in dominant dispersion mechanisms across varying  $Pe$ , results in multiple regimes in the  $\kappa - Pe$  curve. (iii) We show that changes in topology counteract the effects of pore-size reduction by limiting the increase in flow disorder as the degree of compaction increases. Thus, the impact of compaction on dispersion involves mechanical physics rather than merely a reduction in porosity. This study is limited in its ability to capture transient solute transport coupled with structural deformation and does not resolve the influence of compaction on transverse dispersion. Future work should incorporate these factors to enhance the present study. Nevertheless, our findings offer valuable insights into the design and modulation of dispersion coefficients in packed granular materials.

## STATEMENTS AND DECLARATIONS

### Supplementary Material

Supplementary Material for this paper is available to download [here](#).

### Acknowledgements

We are grateful to the editorial board of Interpore Journal for inviting us to revise and submit the content of our academic presentation from Interpore 2024, Qingdao and to compete for the Invited Best Student Paper Award. Expanding upon our earlier work (31), the authors have further refined the study and uncovered additional insights in this paper.

### Author Contributions

**Yang Liu:** Investigation, Software, Simulation and analysis, Visualization, Manuscript draft and revision. **Wenbo Gong:** Investigation, Resources, Manuscript revision. **Han Xiao:** Investigation, Manuscript revision. **Moran Wang:** Supervision, Funding Acquisition, Conceptualization, Methodology, Reviewing.

### Conflicts of Interest

The authors have no conflicts of interest to declare.



## Data, Code & Protocol Availability

Data and codes can be provided upon request.

## Funding Received

This work is financially supported by the NSF grant of China (No. 12432013, U24B6003).

## ORCID IDs

Yang Liu

 <https://orcid.org/0009-0000-2300-9436>

Moran Wang

 <https://orcid.org/0000-0002-0112-5150>

## REFERENCES

1. Amooie, M. A., Soltanian, M. R., & Moortgat, J. (2018). Solutal convection in porous media: Comparison between boundary conditions of constant concentration and constant flux. *Physical Review E*, 98(3), 033118. <https://doi.org/10.1103/PhysRevE.98.033118>
2. Babaei, M., & Joekear-Niasar, V. (2016). A transport phase diagram for pore-level correlated porous media. *Advances in Water Resources*, 92, 23–29. <https://doi.org/10.1016/j.advwatres.2016.03.014>
3. Bear, J. (1988). *Dynamics of fluids in porous media*. Dover publications.
4. Bijeljic, B., & Blunt, M. J. (2007). Pore-scale modeling of transverse dispersion in porous media. *Water Resources Research*, 43(12), 2006WR005700. <https://doi.org/10.1029/2006WR005700>
5. Bijeljic, B., Mostaghimi, P., & Blunt, M. J. (2011). Signature of non-Fickian solute transport in complex heterogeneous porous media. *Physical Review Letters*, 107(20), 204502. <https://doi.org/10.1103/PhysRevLett.107.204502>
6. Bijeljic, B., Muggeridge, A. H., & Blunt, M. J. (2004). Pore-scale modeling of longitudinal dispersion. *Water Resources Research*, 40(11), 2004WR003567. <https://doi.org/10.1029/2004WR003567>
7. Bolster, D. (2014). The fluid mechanics of dissolution trapping in geologic storage of CO<sub>2</sub>. *Journal of Fluid Mechanics*, 740, 1–4. <https://doi.org/10.1017/jfm.2013.531>
8. Bonazzi, A., Jha, B., & De Barros, F. P. J. (2021). Transport analysis in deformable porous media through integral transforms. *International Journal for Numerical and Analytical Methods in Geomechanics*, 45(3), 307–324. <https://doi.org/10.1002/nag.3150>
9. Boon, M., Bijeljic, B., & Krevor, S. (2017). Observations of the impact of rock heterogeneity on solute spreading and mixing. *Water Resources Research*, 53(6), 4624–4642. <https://doi.org/10.1002/2016WR019912>
10. Bruderer, C., & Bernabé, Y. (2001). Network modeling of dispersion: Transition from Taylor Dispersion in homogeneous networks to mechanical dispersion in very heterogeneous ones. *Water Resources Research*, 37(4), 897–908. <https://doi.org/10.1029/2000WR900362>
11. Charlaix, E., Hulin, J. P., & Plona, T. J. (1987). Experimental study of tracer dispersion in sintered glass porous materials of variable compaction. *The Physics of Fluids*, 30(6), 1690–1698. <https://doi.org/10.1063/1.866234>
12. Chen, Z., Jin, X., & Wang, M. (2018). A new thermo-mechanical coupled DEM model with non-spherical grains for thermally induced damage of rocks. *Journal of the Mechanics and Physics of Solids*, 116, 54–69. <https://doi.org/10.1016/j.jmps.2018.03.023>
13. Cundall, P. A., & Strack, O. D. L. (1979). A discrete numerical model for granular assemblies. *Géotechnique*, 29(1), 47–65. <https://doi.org/10.1680/geot.1979.29.1.47>
14. Dentz, M., Hidalgo, J. J., & Lester, D. (2023). Mixing in porous media: Concepts and approaches across scales. *Transport in Porous Media*, 146(1–2), 5–53. <https://doi.org/10.1007/s11242-022-01852-x>
15. Dong, H., & Blunt, M. J. (2009). Pore-network extraction from micro-computerized-tomography images. *Physical Review E*, 80(3), 036307. <https://doi.org/10.1103/PhysRevE.80.036307>
16. Goirand, F., Le Borgne, T., & Lorthois, S. (2021). Network-driven anomalous transport is a fundamental component of brain microvascular dysfunction. *Nature Communications*, 12(1), 7295. <https://doi.org/10.1038/s41467-021-27534-8>
17. Goldobin, D. S. (2011). Scaling of transport coefficients of porous media under compaction. *EPL (Europhysics Letters)*, 95(6), 64004. <https://doi.org/10.1209/0295-5075/95/64004>
18. Gong, W., Chen, Z., Lei, W., Zheng, J., Ju, Y., & Wang, M. (2024). Spontaneous imbibition in dual permeable media using dynamic pore network model. *Journal of Geophysical Research: Solid Earth*, 129(9), e2024JB029002. <https://doi.org/10.1029/2024JB029002>
19. Guéguen, Y., Palciauskas, V., & Guéguen, Y. (1994). *Introduction to the physics of rocks*. Princeton Univ. Press.
20. Hamamoto, S., Perera, M. S. A., Resurreccion, A., Kawamoto, K., Hasegawa, S., Komatsu, T., & Moldrup, P. (2009). The solute diffusion coefficient in variably compacted, unsaturated volcanic ash soils. *Vadose Zone Journal*, 8(4), 942–952. <https://doi.org/10.2136/vzj2008.0184>



21. Hulin, J. P., Charlaix, E., Plona, T. J., Oger, L., & Guyon, E. (1988). Tracer dispersion in sintered glass beads with a bidisperse size distribution. *AIChE Journal*, 34(4), 610–617. <https://doi.org/10.1002/aic.690340410>
22. Kandhai, D., Hlushkou, D., Hoekstra, A. G., Slood, P. M. A., Van As, H., & Tallarek, U. (2002). Influence of stagnant zones on transient and asymptotic dispersion in macroscopically homogeneous porous media. *Physical Review Letters*, 88(23), 234501. <https://doi.org/10.1103/PhysRevLett.88.234501>
23. Kang, P. K., Lei, Q., Dentz, M., & Juanes, R. (2019). Stress-induced anomalous transport in natural fracture networks. *Water Resources Research*, 55(5), 4163–4185. <https://doi.org/10.1029/2019WR024944>
24. Khan, Z. A., Agnaou, M., Sadeghi, M. A., Elkamel, A., & Gostick, J. T. (2021). Pore network modelling of galvanostatic discharge behaviour of lithium-ion battery cathodes. *Journal of The Electrochemical Society*, 168(7), 070534. <https://doi.org/10.1149/1945-7111/ac120c>
25. Khrapitchev, A. A., & Callaghan, P. T. (2003). Reversible and irreversible dispersion in a porous medium. *Physics of Fluids*, 15(9), 2649–2660. <https://doi.org/10.1063/1.1596914>
26. Koch, D. L., & Brady, J. F. (1985). Dispersion in fixed beds. *Journal of Fluid Mechanics*, 154, 399–427. <https://doi.org/10.1017/S0022112085001598>
27. Kumar, A., Jaiswal, D. K., & Kumar, N. (2009). Analytical solutions of one-dimensional advection-diffusion equation with variable coefficients in a finite domain. *Journal of Earth System Science*, 118(5), 539–549. <https://doi.org/10.1007/s12040-009-0049-y>
28. Kuncoro, P. H., Koga, K., Satta, N., & Muto, Y. (2014). A study on the effect of compaction on transport properties of soil gas and water I: Relative gas diffusivity, air permeability, and saturated hydraulic conductivity. *Soil and Tillage Research*, 143, 172–179. <https://doi.org/10.1016/j.still.2014.02.006>
29. Liu, F., & Wang, M. (2022). Phase diagram for preferential flow in dual permeable media. *Journal of Fluid Mechanics*, 948, A19. <https://doi.org/10.1017/jfm.2022.649>
30. Liu, Y., Gong, W., Xiao, H., & Wang, M. (2024a). A pore-scale numerical framework for solute transport and dispersion in porous media. *Advances in Water Resources*, 183, 104602. <https://doi.org/10.1016/j.advwatres.2023.104602>
31. Liu, Y., Gong, W., Xiao, H., & Wang, M. (2024b). Non-monotonic effect of compaction on longitudinal dispersion coefficient of porous media. *Journal of Fluid Mechanics*, 988, R2. <https://doi.org/10.1017/jfm.2024.454>
32. Liu, Y., Gong, W., Zhao, Y., Jin, X., & Wang, M. (2022). A pore-throat segmentation method based on local hydraulic resistance equivalence for pore-network modeling. *Water Resources Research*, 58(12), e2022WR033142. <https://doi.org/10.1029/2022WR033142>
33. Mehmani, Y., & Balhoff, M. T. (2015). Eulerian network modeling of longitudinal dispersion. *Water Resources Research*, 51(10), 8586–8606. <https://doi.org/10.1002/2015WR017543>
34. Molina, O., Vilarrasa, V., & Zeidouni, M. (2017). Geologic carbon storage for shale gas recovery. *Energy Procedia*, 114, 5748–5760. <https://doi.org/10.1016/j.egypro.2017.03.1713>
35. Morris, J. P., Hao, Y., Foxall, W., & McNab, W. (2011). A study of injection-induced mechanical deformation at the In Salah CO<sub>2</sub> storage project. *International Journal of Greenhouse Gas Control*, 5(2), 270–280. <https://doi.org/10.1016/j.ijggc.2010.10.004>
36. Östergren, K. C. E., & Trägårdh, C. (2000). Characterization of hydrodynamic dispersion in a chromatographic column under compression. *Chemical Engineering Journal*, 79(2), 103–111. [https://doi.org/10.1016/S1385-8947\(00\)00165-0](https://doi.org/10.1016/S1385-8947(00)00165-0)
37. Patzek, T. W., & Silin, D. B. (2001). Shape factor and hydraulic conductance in noncircular capillaries. *Journal of Colloid and Interface Science*, 236(2), 295–304. <https://doi.org/10.1006/jcis.2000.7413>
38. Peters, G. P., & Smith, D. W. (2002). Solute transport through a deforming porous medium. *International Journal for Numerical and Analytical Methods in Geomechanics*, 26(7), 683–717. <https://doi.org/10.1002/nag.219>
39. Pfannkuch H. O. (1963), Contribution a l'etude des deplacement de fluids miscible dans un milieu poreux. [Contribution to the study of miscible fluid flow in porous media]. *Revue de l'Institut Francais du Petrole* [Journal of the French Petroleum Institute] 18(2), 215–270. <https://search.worldcat.org/fr/title/Contribution-a-l-etude-des-deplacements-de-fluides-miscibles-dans-un-milieu-poreux/oclc/460735531>
40. Potyondy, D. O., & Cundall, P. A. (2004). A bonded-particle model for rock. *International Journal of Rock Mechanics and Mining Sciences*, 41(8), 1329–1364. <https://doi.org/10.1016/j.ijrmms.2004.09.011>
41. Puyguiraud, A., Gouze, P., & Dentz, M. (2019). Stochastic dynamics of lagrangian pore-scale velocities in three-dimensional porous media. *Water Resources Research*, 55(2), 1196–1217. <https://doi.org/10.1029/2018WR023702>
42. Puyguiraud, A., Gouze, P., & Dentz, M. (2021). Pore-scale mixing and the evolution of hydrodynamic dispersion in porous media. *Physical Review Letters*, 126(16), 164501. <https://doi.org/10.1103/PhysRevLett.126.164501>

43. Qiu, J., Chen, X., & Tong, J. (2022). Fully transient analytical solution for solute transport in 1D deforming saturated porous media considering nonlinear compressibility and permeability. *Applied Mathematical Modelling*, 108, 122–141. <https://doi.org/10.1016/j.apm.2022.03.002>
44. Ranjith, P. G., & Perera, M. S. A. (2011). A new triaxial apparatus to study the mechanical and fluid flow aspects of carbon dioxide sequestration in geological formations. *Fuel*, 90(8), 2751–2759. <https://doi.org/10.1016/j.fuel.2011.04.004>
45. Reynolds, A. M., Reavell, S. V., & Harral, B. B. (2000). Flow and dispersion through a close-packed fixed bed of spheres. *Physical Review E*, 62(3), 3632–3639. <https://doi.org/10.1103/PhysRevE.62.3632>
46. Ringrose, P. S., Mathieson, A. S., Wright, I. W., Selama, F., Hansen, O., Bissell, R., Saoula, N., & Midgley, J. (2013). The in salah CO<sub>2</sub> storage project: Lessons learned and knowledge transfer. *Energy Procedia*, 37, 6226–6236. <https://doi.org/10.1016/j.egypro.2013.06.551>
47. Sahimi, M. (2011). *Flow and transport in porous media and fractured rock: From classical methods to modern approaches* (2nd ed). John Wiley & Sons, Incorporated.
48. Sahimi, M., Hughes, B. D., Scriven, L. E., & Ted Davis, H. (1986). Dispersion in flow through porous media—I. One-phase flow. *Chemical Engineering Science*, 41(8), 2103–2122. [https://doi.org/10.1016/0009-2509\(86\)87128-7](https://doi.org/10.1016/0009-2509(86)87128-7)
49. Sahimi, M., & Imdakm, A. O. (1988). The effect of morphological disorder on hydrodynamic dispersion in flow through porous media. *Journal of Physics A: Mathematical and General*, 21(19), 3833–3870. <https://doi.org/10.1088/0305-4470/21/19/019>
50. Smith, D. W. (2000). One-dimensional contaminant transport through a deforming porous medium: Theory and a solution for a quasi-steady-state problem. *International Journal for Numerical and Analytical Methods in Geomechanics*, 24(8), 693–722. [https://doi.org/10.1002/1096-9853\(200007\)24:8<693::AID-NAG91>3.0.CO;2-E](https://doi.org/10.1002/1096-9853(200007)24:8<693::AID-NAG91>3.0.CO;2-E)
51. Tian, Z., Zhang, D., Zhou, G., Zhang, S., & Wang, M. (2023). Compaction and sintering effects on scaling law of permeability-porosity relation of powder materials. *International Journal of Mechanical Sciences*, 256, 108511. <https://doi.org/10.1016/j.ijmecsci.2023.108511>
52. Vaclav Smilauer, Angelidakis, V., Catalano, E., Caulk, R., Chareyre, B., et al. (2021). *Yade documentation*. Zenodo. <https://doi.org/10.5281/ZENODO.5705394>
53. Zhang, D., Tian, Z., Chen, Z., Wu, D., Zhou, G., et al. (2020). Compaction effects on permeability of spherical packing. *Engineering Computations*, 37(9), 3079–3096. <https://doi.org/10.1108/EC-01-2020-0015>
54. Zhu, W., Khirevich, S., & Patzek, T. W. (2021). Impact of fracture geometry and topology on the connectivity and flow properties of stochastic fracture networks. *Water Resources Research*, 57(7), e2020WR028652. <https://doi.org/10.1029/2020WR028652>